Steric construction and modulation of Co–N$_x$ single-atom electrocatalysts via polyoxometalate clusters integration

Yunping Wu [1], Shuwen Niu [1], Zhengyu Wei, Lingzhe Meng, Wei Wei [*]

Department of Applied Chemistry, School of Chemistry, Xi'an Jiaotong University, Engineering Research Center of Energy Storage Materials and Devices, Ministry of Education, Xi'an Key Laboratory of Sustainable Energy Material Chemistry, Xi'an 710049, PR China

ARTICLE INFO

ABSTRACT

Single-atom catalysts (SACs) with nitrogen-coordinated transition metal sites (M-N$_x$) hold great promise for electrocatalytic oxygen reduction and oxygen evolution reactions (ORR, OER). Despite substantial achievements based on the confinement pyrolysis and heteroatom-doping methods, the M-N$_x$ SACs still suffer from low yield of atomic sites and less tenability of electronic states of M-N$_x$ center. Here, an innovate synthesis methodology is proposed for surface integrating Co atoms onto polyoxometalate (POM) and its derivative clusters, which promise to regulate the atomic distribution and coordination environments of Co-N$_x$ SACs at the sub-nanometer level. The synthetic procedures exhibit general applicability for a variety of POM clusters to achieve high atomic Co loading up to 9.9 wt%. Steric integration by POM-derived clusters (e.g. MoN) also impart strengthened d-p orbital hybridization of Co-N$_x$ SACs by the formation of Co-N-Mo bonding, which surpass common heteroatoms toward modulating the geometric and electronic structures of M-N$_x$ SACs, leading to pronounced catalytic activity and durability. This work validates the effectiveness of the unique POM-integration strategy toward atomic dispersion of transition metal, further guides the engineering of M-N$_x$ SACs to promote catalytic performance from the sub-nanometer scale.

1. Introduction

Single-atom catalysts (SACs) demonstrate the advantages of maximum atom utilization, superior catalytic activity and selectivity, which offer a promising route for developing sustainable energy conversion and storage systems, such as fuel cells [1,2] and metal-air batteries [3,4]. The oxygen reduction reaction (ORR) is a key process which plays a dominate role on the performance of aforementioned devices [5]. However, the sluggish kinetics of ORR and dependence on expensive Pt-based catalysts have hindered the energy storage efficiency and their widespread application [6,7]. Single transitional metal atom supported on N-doped carbon matrices (M-N$_x$, M=Fe, Co and Ni) is among the most promising SACs for replacing Pt, taking advantage of its high electrocatalytic activity, low cost and good stability for catalyzing ORR [8–11]. It is generally recognized that the coordinating N atoms can adjust the charge density and the d orbital states of the metal center, rendering intrinsic ORR activity of M-N$_x$ sites [12,13].

Atomic dispersion of the transition metal atoms in high dense constitutes the key character of M-N$_x$ SACs that promises high electrocatalytic activity, yet it has been greatly hampered by the synthetic approaches [14]. Pyrolysis of the precursors containing transition metal, nitrogen and carbon sources is a simple and cost-effective method [15–17], but fails to confine the isolated metal center at atomic scale, resulting in large amounts of inactive agglomeration with less-active sites during calcination [18–20]. Recently, metal-organic frameworks (MOFs) have been widely acknowledged and used as ideal template for producing M-N$_x$ SACs [21,22]. It is proved that transition metal atoms can be trapped via steric coordinative bonding or porous structure of MOFs [23], which promote transition of M-N$_x$ sites against undesired aggregation during pyrolysis. However, the yield of M-N$_x$ atomic sites derived from MOFs is still low (<5 wt%) and uncontrollable, also certain amount of sites spread over the microporous regions, which decrease the utilization of active sites. In addition, the intrinsic activity of the established M-N$_x$ SACs is critically dependent on the coordination environment of metal centers. To date, heteroatomic doping (e.g. B, S, P) has been extensively studied to optimize the electron distribution and properties of M-N$_x$ sites by regulation of coordination atoms/numbers and configurations [24–26]. Nevertheless, due to the limited

---

hybridization between M-N$_x$ centers and the heteroatoms, as well as common carbonaceous support, the heteroatom doping method poses fundamental restrictions on tuning local environment in terms of the charge transfer and redistribution, and avoiding aggregation of single metal atoms in operation.

In this study, a cluster integration strategy is proposed as a new methodology to boost the density and intrinsic activity of M-N$_x$ active sites from sub-nanometer scale. Polyoxometalates (POMs) with oxygen-enriched surface ligands are used as the versatile mediators to integrate Co atoms onto POM clusters, and prevents migration of Co atoms during pyrolysis to endow abundant Co-N$_x$ single-atom sites surrounding the POM-derived clusters. It exhibits general applicability for a variety of POM clusters to integrate Co atoms onto POM clusters and maintain atomic dispersion around POM derivative clusters during pyrolysis. Different form the conventional heteroatom coordinated structures, the POM-derived clusters (e.g. MoN) establish rigid Co-N-Mo coordinative linkages with Co-N$_x$ centers based on the C$_3$N$_4$ matrix, and provide an opportunity to modulate the coordination environment of Co-N$_x$ sites from the sub-nanometer scale. Remarkably, the loading content of atomic Co integrated by POM derivative clusters reaches up to 9.9 wt%, which demonstrates a viable route toward maximizing the density and utilization of the atomic metal sites in M-N$_x$ SACs. Compared with common heteroatom doping, the POM derivative cluster (MoN) could strengthen d-p orbital hybridization and induce significant d-band broadening and downshift of Co centers, enabling optimization of adsorption properties for intermediates and promotion of intrinsic activity. Consequently, the activity and stability from the cluster-integrated Co-N$_x$ SACs outperform the analogous electrocatalysts prepared by heteroatom doping approach previously, which is of great specificity endowed by the POM and derivative clusters to engineer M-N$_x$ SACs at sub-nanometer scale.

2. Experimental section

2.1. Materials and synthesis

2.1.1. Materials

Urea (H$_2$NCONH$_2$, 99%, powder), melamine (C$_3$H$_6$N$_6$, 99.9%, powder), Cobalt nitrate hexahydrate (Co(NO$_3$)$_2$·6H$_2$O, 99%, pellets), Ammonium heptamolybdate tetrahydrate ((NH$_4$)$_6$Mo$_7$O$_{24}$, 99%, powder), Ammonium tungstate ((NH$_4$)$_5$H$_5$[H$_2$W$_6$O$_{24}$]), 99%, powder), Sodium dodecatungstophosphate hydrate (Na$_3$PW$_{12}$O$_{40}$, 99%, powder), Potassium hydroxide (KOH, 90%, pellets) are purchased from Aladdin. 5 wt% Nafion solution is bought from Sigma-Aldrich. 20% Pt/C catalyst are bought from Shanghai Hesen Corporation. Zn electrode (thickness of 0.2 mm) are purchased from Changsha Spring Corporation. Deionized water is used throughout the experiments. All the materials are used as received.

2.1.2. Synthesis of ECTA and CTA supramolecular substrates

Urea (6 g) and melamine (3 g) were dissolved in 50 mL water in sequence. After stirring at room temperature for 12 h, the mixed solution was transferred to Teflon-lined stainless steel autoclave and kept at 180°C for 10 h. The products were collected and rinsed three times with large amounts of deionized water, and dried in a vacuum oven at 60°C for 12 h, giving rise to the lamellar conjugated triazine with expanded interlayer spacing (ECTA substrate). For comparison, a lamellar conjugated triazine was also prepared by phosphorous acid-assisted hydrothermal method. Typically, phosphoric acid (1.2 g) and melamine (1 g) were dissolved in 100 mL deionized water at 80 °C. Then the mixed solution was transferred to Teflon-lined stainless steel autoclave and kept at 180°C for 10 h. The products were collected and rinsed with deionized water three times, and dried in a vacuum oven at 60°C for 12 h, obtaining the conjugated triazine assembly (CTA substrate).

2.1.3. Synthesis of Co-ECTA, Mo$_7$-ECTA, and various POM-Co-ECTA precursors

The ECTA substrate was firstly dispersed in 30 mL deionized water, then 40 mg of Co(NO$_3$)$_2$ was added. The resultant solution was stirred under reflux condition for 12 h at 140 °C, and then the product was washed three times and dried, giving rise to the Co-ECTA precursor. The Mo$_7$-ECTA precursor was synthesized following the same synthetic procedures by replacing Co(NO$_3$)$_2$ with (NH$_4$)$_6$Mo$_7$O$_{24}$ salt. Based on the synthetic procedures of Co-ECTA, different POM clusters including (NH$_4$)$_6$Mo$_7$O$_{24}$, (NH$_4$)$_5$H$_5$[H$_2$W$_6$O$_{24}$]), Na$_3$PW$_{12}$O$_{40}$, Na$_2$V$_6$O$_{16}$ were added into above Co-ECTA solution and kept under reflux reaction at 140 °C for 12 h. The products were washed three times and dried, giving rise to the POM-modulated Co-ECTA precursors, which were designated as Mo$_7$-Co-ECTA, W$_6$-Co-ECTA, W$_{12}$-Co-ECTA and V$_6$-Co-ECTA, respectively.

2.1.4. Preparation of cluster-integrated Co-N$_X$ SACs

The cluster-integrated SACs were obtained by pyrolysis of the various POM-Co-ECTA precursors under Ar/H$_2$ (v/v=95/5%) atmosphere. Typically, the precursors of Mo$_7$-Co-ECTA, W$_6$-Co-ECTA, W$_{12}$-Co-ECTA and V$_6$-Co-ECTA were heated into 570 °C in a tube furnace with a heating rate of 2 °C min-1 and kept at the temperature for 2 h, giving birth to SACs of Co-MoN@PCN, Co-WN@PCN-6, Co-WN@PCN-12 and Co-VN@PCN, respectively. For the purpose of comparison, the catalysts of Co@PCN and MoN@CN were synthesized following the same pyrolysis process by calcining Co-ECTA and Mo$_7$-ECTA precursors, respectively.

2.1.5. Test of single atom content in catalysts

In order to detect the single atoms content in the Co−N−C SACs, the resultant Co@PCN, Co-MoN@PCN, Co-WN@PCN-6, Co-WN@PCN-12 and Co-VN@PCN were separately dispersed in 0.5 M H$_2$SO$_4$ solution under stirring for 24 h at room temperature and then wash with deionized water; subsequently, the acidized catalysts were dried and accurately weighed and then dispersed in chloroazotic acid till achieved sufficient dissolution. Finally, the mixed chloroazotic acid solutions were diluted for testing the Co contents and other metal contents.

2.2. Structural characterizations

The high-angle annular dark-field scanning TEM images (HAADF-STEM) and elemental distribution were acquired from a Lorenz Transmission Electron Microscope (ThermoFisher, Talos-F200X) with Energy-dispersive X-ray spectrometer (EDS). Morphology and lattice fringes of all samples were collected using a transmission electron microscope (TEM, JEM-F200, JEOL). Structural characterization and analysis of Co-MoN@PCN were carried out using a concentrating spherical aberration-corrected electron microscope (ARM200F, JEOL). The micromorphology and elemental mapping image of all the samples were characterized via a field emission scanning electron microscope (FESEM, HT7700) and EDS. The chemical structure of the samples were examined by an X-ray diffraction (XRD) meter (D8 ADVANCE, Bruker) equipped with Cu Ka radiation (λ=0.1541 nm). The valence state and bonding state of elements in the samples were tested using an X-ray photoelectron spectroscopy (XPS) system (ESCALAB Xi$^+$, Thermo-Scientific). The data were calibrated using C 1 s at 284.6 eV as the reference. The X-ray absorption spectra measurements for the Co-edge were conducted in transmission mode on beamline of TPS44A1 in the in National Synchrotron Radiation Research Center (NSRRC), Taiwan. XANES and EXAFS data reduction and analysis were analyzed by Athena and Artemis software, and the wavelet transforms for the k^2-weighted EXAFS signal were fitted with Hama software. An infrared spectrum (IR) was recorded on a Fourier transform IR spectrometer (FTIRPE-2000, the United States). The Raman spectra were recorded using a Raman spectrometer (Raman, hr800). The actual content of Co and other metals in the catalyst were tested by inductively coupled plasma mass

spectrometry (ICP-MS, NEXlON 350D). The specific surface area of the sample was investigated by a Brunauer-Emmett-Teller (BET) using a N_2 adsorption–desorption instrument (ASAP2020 Plus HD88).

2.3. Tests of electrocatalytic performance

2.3.1. ORR test

The catalyst ink was prepared by dispersing 4 mg of catalyst into mixture solution containing 490 µL ethanol, 490 µL water and 20 µL 5 wt % Nafion. Then, the ink was sonicated to maximum disperse. Subsequently, 20 µL of the catalyst was loaded onto a rotating disc electrode (RDE) with a 5 mm diameter (loading amount: 4 µg cm^{-2}). Finally, the dried RDE electrode was used as the working electrode. Electrochemical measurements were conducted in a standard three electrode system with a graphite rod counter and Hg/HgO reference electrode. LSV measurements were conducted with scan rate of 5 mV s^{-1}. For the ORR at a RDE, the electron transfer number (n) was calculated by Koutechy-Levich (K-L) formula:

$$\frac{1}{j} = \frac{1}{j_L} + \frac{1}{j_K} = \frac{1}{B\omega^{1/2}} + \frac{1}{j_K} \tag{1}$$

Where: j is the measured current density; j_L and j_K represent the diffusion-limiting and kinetic current densities, respectively; ω is the angular velocity (rpm). The K-L curves was used to calculated the value of B. The number of electrons transferred further were obtained according the following equation:

$$B = 0.62nFC_0(D_0)^{2/3}v^{-1/6} \tag{2}$$

Where: n represents is the electron transfer number, F is Faraday constant (96485 C mol^{-1}) and C_0 is the bulk concentration of O_2 (1.2×10^{-3} M). In 0.1 M KOH, ν and D_0 are the kinetic viscosity (0.01 cm^2 s^{-1}) and diffusion coefficient of O_2 (1.9×10^{-5} cm^2 s^{-1}); The rotating ring-disk electrode (RRDE) measurement was record at a scan rate of 5 mV s^{-1} in an O_2-saturated 0.1 M KOH electrolyte and the ring electrode potential was set to 1.2 V vs. RHE. The hydrogen peroxide yield (%H_2O_2) and the electron transfer number (n) were calculated by the following equations:

$$\%H_2O_2 = 200 \times \frac{I_R/N}{I_D + I_R/N} \tag{3}$$

$$n = 4 \times \frac{I_D}{I_D + I_R/N} \tag{4}$$

Where: I_D represents the disk current; I_R represents the ring current; N is the collection efficiency of the platinum ring (0.37).

The electrochemical active area (ECSA) can be obtained based on double layer capacitance (C_{dl}). The C_{dl} was test via CV curves of the electrode at a non-Faradic region of 1.0–1.1 V with different scan (5, 10, 15, 20, and 25 mV s^{-1}). The slope of the above profiles was C_{dl}. The ECSA of the catalyst can be calculated according to the Eqs. (5–6)

$$j = \nu C_{dl} \tag{5}$$

$$ECSA = \frac{C_{dl}}{C_s} \tag{6}$$

Where C_{dl} is the electrochemical double-layer capacitance, C_s is the specific capacitance of the sample, the value of C_s is 0.04 mF cm^{-2} in this calculation according to typical report [27], and ν is the sweep speed.

2.3.2. Methanol tolerance and durability test

The methanol tolerance of the catalyst was assessed by the current-time (I-T) chronoamperometric response which recorded the current variation before and after adding methanol at 1000 s. To evaluate the durability, the accelerated CV test was performed in 0.1 M O_2-saturated

KOH solution for 20,000 cycles, with a voltage range of 0.7 and 1.1 V (vs. RHE) at a sweep speed of 100 mV s^{-1}. After durability test, the catalyst on the working electrode was ultrasonically collected by water for further structural characterizations. Cyclic stability was also tested by i-t method. The potential was fixed at 0.7 V (vs. RHE) for 90,000 s and the loss of current density was then measured.

2.3.3. OER test

OER catalytic performance were tested in an oxygen-saturated 0.1 M KOH electrolyte with a voltage range of 1.2–1.8 V (vs. RHE), a scan rate of 5 mV s^{-1} based on a standard three-electrode. A rotation speed of 1600 rpm was used to acquire LSV curves of the catalysts during OER process.

2.3.4. Test of electrocatalyst as cathode in Zinc-air batteries (ZABs)

The aqueous Zn-air batteries (ZABs) were assembled with polished zinc plates as anode, the Co-MoN@PCN or commercial Pt/C (20 wt%) coated on 1 cm^2 carbon paper coupled with a hydrophobic gas layer as the air cathode, 0.2 M $Zn(NO_3)_2$ and 6 M KOH mixed solution as the electrolyte. The open circuit potential and charge/discharge polarization curves were collected on a CHI 760E workstation at the scan rate of 5 mV s^{-1}. The specific capacitance of the ZABs were measured by the constant current density discharge of 10 mA cm^{-2}, and the mass of the zinc sheet before and after the test was weighed respectively to calculate the specific capacity of the ZABs. The current density increases from 5 mA cm^{-2} to 10 mA cm^{-2}, 20 mA cm^{-2}, 50 mA cm^{-2} and then decreases to 5 mA cm^{-2} by E-t method. The constant current charge-discharge stability test was carried out on a multi-channel Land electrochemical test system. The current density was 5 mA cm^{-2}, and the discharge time and charge time were both set to 5 min to determine the constant current charge-discharge characteristics of ZABs.

2.4. Computational details

Calculations based on first-principles density functional theory (DFT), including molecular dynamics simulations were executed utilizing the Vienna Ab initio Simulation Package (VASP) in conjunction with the Projector Augmented Wave (PAW) methodology. The exchange-correlation functional was managed within the parameters of the Generalized Gradient Approximation (GGA), adopting the Perdew-Burke-Ernzerhof (PBE) functional. We implemented a plane wave basis set with an energy cutoff set at 500 eV, and the geometric relaxation was carried through until the forces acting on each atom were less than 0.03 eV/Å. The sampling of the Brillouin zone was conducted using a $2 \times 2 \times 1$ k-point grid. To assure rigorous consistency, calculations were performed until the energy convergence threshold was less than 10^{-5} eV. To effectively isolate periodic structures and preclude their interaction, a vacuum buffer of 15 Å was inserted along the z-axis.

The free energy of the intermediates is calculated at U=0 V and pH = 13, U=0.4603 V and pH = 13.

$$\Delta G = \Delta E_{DFT} + \Delta ZPE - T\Delta S \tag{7}$$

where ΔE_{DFT}, ΔZPE and ΔS are the changes of the reaction energy obtained from DFT calculations, zero-point energy, and the changes of entropy from the initial state to the final state, respectively. T is temperature and the T of 298.15 K was used in all computations.

3. Results and discussion

3.1. Steric integration and characterizations of Co—Nx single-atom electrocatalyst

The synthetic schematic of the Co-MoN@PCN catalyst is depicted in Fig. 1. A soft lamellar mediator was firstly constructed by self-assembly of melamine and urea molecules. Under hydrothermal condition,
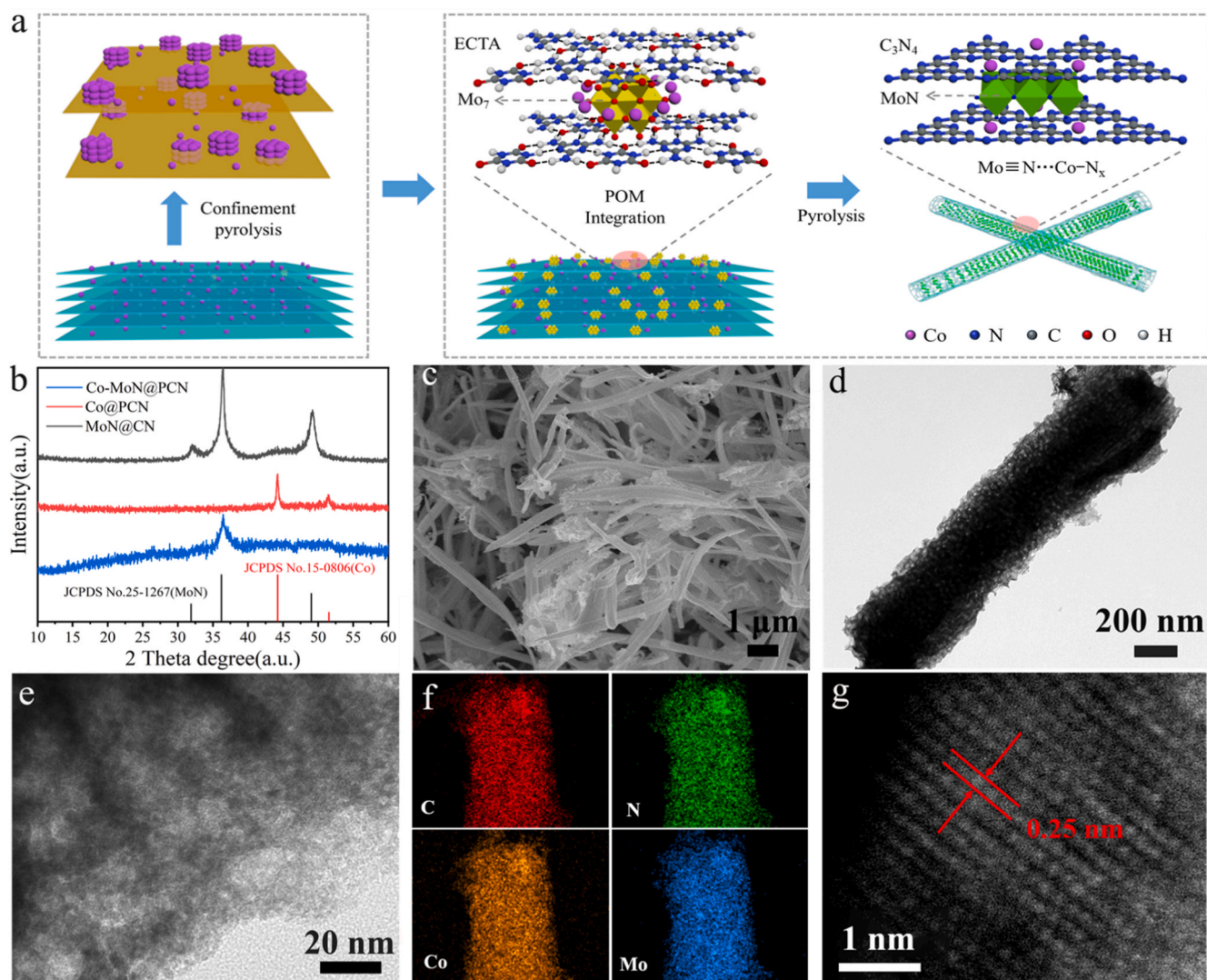
Fig. 1. (a) Schematic illustration of common confinement strategy (left) and cluster-integration strategy in this work (right) for preparation of M-N_x SACs. Structural characterizations of the Co-MoN@PCN catalyst: (b) XRD patterns, (c) SEM image, (d) TEM image, (e) magnified TEM image, (f) elemental mapping images, (g) aberration-corrected HAADF-STEM image.

melamine was partly hydrolyzed and cross-linked into lamellar conjugated triazine (CTA) via intermolecular hydrogen bonding. Meanwhile, urea decomposed into a variety of gas to expand the stacking CTA layers, giving rise to expanded CTA mediator (ECTA, Fig. S1). Such an expanded interlayer space facilitates intercalation of different metal precursors to coordinate with the functional groups (e.g., -NH₂, -OH) between ECTA layers, thus providing a suitable platform for creating single-atom metal catalysts (SACs). Typically, ECTA can sufficiently chelate with Co^{2+} to form interlayer-coordinated Co(II)-ECTA precursor (Co-ECTA, Fig. 1a-left). Pyrolysis of this precursor renders numerous atomic Co-N_x sites that supported on porous C_3N_4 frameworks (Co@PCN). Such a confinement strategy is presently the most used method to produce the M-N_x SCAs, but still suffers from low yield of the single atomic sites and limited tenability. Herein, we establish an alternative protocol for coordinative trapping and integration of Co(II) by series of POM clusters, which enable to boost single atomic dispersion and tune electronic structure of Co-N_x sites at sub-nanometer levels. Particularly revealed in Fig. 1a-right, Co(II) and $(NH_4)_6Mo_7O_{24}$ clusters (Mo_7) could stepwise intercalate into ECTA to form nanofibrous Mo_7-Co-ECTA precursor (Fig. S2), and subsequently transformed into unique cluster-integrated SACs by pyrolysis. The synergism of POM clusters and ECTA dictated surface integration and confinement of Co-N_x sites

around MoN clusters, which consequently promoted the atomic distribution and durability of Co-N_x sites based on C_3N_4 matrix (Co-MoN@PCN). For the purpose of comparison, bare Mo_7 clusters could be intercalated into ECTA alone for the preparation of MoN@CN catalyst base on the same procedures (see details in the experimental section).

The chemical structure of as-prepared Co@PCN, Co-MoN@PCN and MoN@CN catalysts were probed by XRD. In Fig. 1b, the Co@PCN exhibits clear diffraction peaks appeared at $2\theta = 44.2°$ and $51.5°$, which are indexed to the (111) and (200) planes of metallic Co (JCPDS No. 15–0806) [28]. The MoN@CN displays characteristic peaks at 31.9 °, 36.2° and 49.0°, which are ascribed to the (002), (200) and (202) planes of MoN (JCPDS No. 25–1367). As a result of homogenous dispersion of MoN grains, the Co-MoN@PCN only exhibits the strongest (200) peak of MoN. It's worth noting that no peak corresponding to metallic cobalt or other metal compound is identified in Co-MoN@PCN, indicating that POM and derivative clusters can efficiently disperse atomic Co(II) during the synthetic processes. The Raman spectra of Co@PCN and Co-MoN@PCN reveal characteristic peaks at 467, 510 and 670 cm^{-1} (Fig. S3a), belonging to the E_g, F_{2g} and A_{1g} vibration modes of Co in the Co-N-C structure [29]. It should be noted that a shoulder peak near to A_{1g} vibration can be discerned for Co-MoN@PCN (Fig. S3b), which is indexed to the Co-N-Mo bonding [30]. Above comparative results

indicate that two types of N-bonding configurations (Co-N-C and Co-N-Mo) exist in the Co-MoN@PCN catalyst. In the FT-IR spectra, the pure PCN presents typical N–H, C≡N and C–N stretching vibrations of g-C_3N_4 heterocycles (Fig. S3c), indicating that ECTA mediator transform to g-C_3N_4 framework through high-temperature polycondensation. It should be noted that the stretching vibrations of C≡N in the three catalysts exhibit slight red-shifts (dipole distance change of C≡N) relative to PCN, which are mainly due to the coordination bonding between metallic atoms (Co and Mo) and N. In the fingerprint region of FT-IR (Fig. S3d), the Co–N vibration peak in Co-MoN@PCN exhibits obvious red shift from 868 cm^{-1} (in Co@PCN) to 857 cm^{-1} [31], revealing different coordinated linkage of Co-N in the two catalysts. Also, the Mo–N peak in Co-MoN@PCN blue-shifts by 18 cm^{-1} with respect to that in MoN@CN (890 cm^{-1}), which is mainly due to the different crystallinity of MoN in the two samples, as indicated in the XRD spectra. In association with Raman characterization, the wave number shifts of Co-N could be attributed to the formation of Co-N-Mo bond in Co-MoN@PCN, by which electrons transfer from Co to Mo using N as a bridge. Therefore, the FT-IR spectroscopy confirmed the strong electronic coupling between Co–N_x and MoN to form interfacial Co–N–Mo bonds in Co-MoN@PCN.

The scanning electron microscopy (SEM) image and transmission electron microscopy (TEM) image of Co-MoN@PCN display uniform cylinder structure with average diameter of ~300 nm (Fig. 1c and 1d). The magnified TEM image (Fig. 1e) reveals that abundant ultrafine clusters with grain size of ~2 nm are homogeneously distributed in porous PCN matrix. In the high-resolution TEM (HRTEM, Fig. S4a), the discerned lattice spacing of 0.25 nm is corresponded to the (200) crystal plane of MoN. No crystalline cobalt or its compound is detected, confirming that Co element is almost atomically dispersed within Co-MoN@PCN catalyst. The microstructure of Co-MoN@PCN was analyzed in detail by high-angle annular dark field scanning transmission electron microscopy (HAADF-STEM). It is clear from Fig. S4b that the cylinder is comprised of ultrathin and small nanosheets which interconnected to form a porous framework. The TEM-energy dispersive X-ray (EDX) elemental mapping images (Fig. 1f and Fig. S4c) confirm the even distribution of C, N, Co, and Mo throughout the cylinder. In contrast, the Co@PCN without POM regulation exhibits a large amount of Co nanoparticles (NPs, with average size of 20 nm) which are closely wrapped by PCN matrix (Fig. S5). These comparative results indicate the Mo_7 and derivative MoN clusters are capable of confining and tuning the spatial distribution of Co(II) to develop new type of SACs. Structural characterizations of MoN@CN reveal a bulk lamellar structure that is decorated with numerous MoN clusters (Fig. S6). The EDX mapping
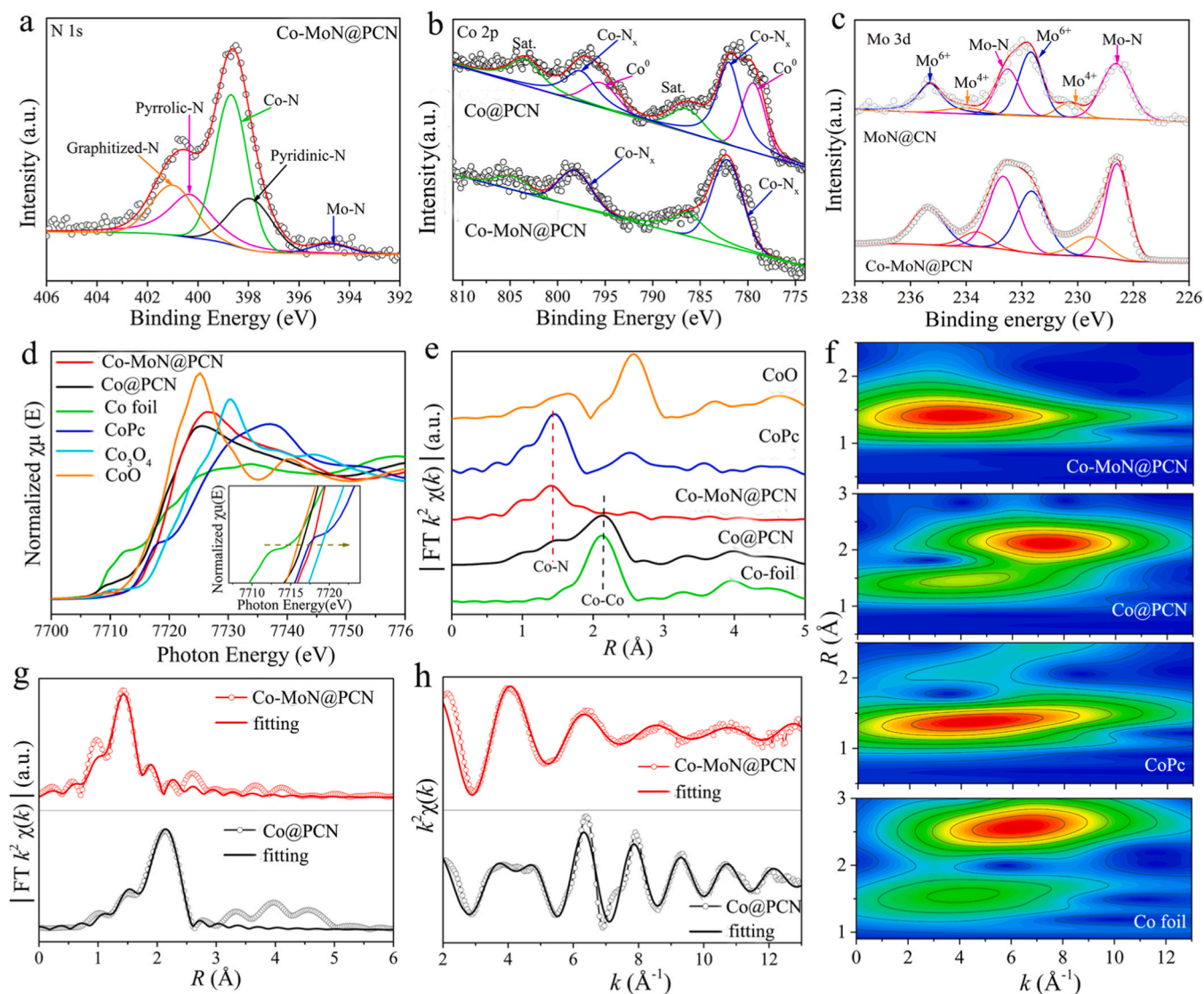

Fig. 2. Spectroscopy characterizations of Co-MoN@PCN and Co@PCN catalysts: the high-resolution (a) N 1 s, (b) Co 2p and (c) Mo 3d XPS spectra; (d) Co K-edge XANES spectra, (e) Fourier-transform (FT) EXAFS curves and (f) WT-EXAFS spectra; the Co K-edge EXAFS spectra with (g) R-space and (h) k-space fitting curves.

images of Co-MoN@PCN in high magnification corroborate uniform distribution of C, N, Co and Mo elements (Fig. S7). Further, the aberration-corrected HAADF-STEM of Co-MoN@PCN manifests the linear bright spots with lattice fringes of 0.25 nm (Fig. 1g), representing the (200) planes of MoN cluster. Similar to HRTEM, no lattice structures derived from Co NPs or other compounds were detected, implying the atomic distribution of Co element around MoN clusters. The line-scan elemental profiles (Fig. S4d) verify distinct intensity of Co element along with the Mo element, indicating the single atomic distribution of Co crossing (002) planes of MoN. The above characterization results show that the Co atoms are incorporated into the surface lattice of MoN clusters, by which significant amount of Co-N$_x$ sites are integrated by MoN clusters.

To distinguish the electronic states surrounding atomically dispersed Co, the chemical structures among three catalysts were investigated by X-ray photoelectron spectroscopy (XPS). The high-resolution N 1 s spectra of Co-MoN@PCN and Co@PCN (Fig. 2a and Fig. S8a) can be deconvoluted into peaks with binding energies at 398.1, 398.6, 400.6 and 403.4 eV, which correspond to pyridinic N, Co−N, pyrrolic N and graphitized N, respectively. Meanwhile, Co-MoN@PCN and MoN@CN exhibits Mo−N signals at 394.8 eV that derived from MoN clusters (Fig. S8b). In the high-resolution Co 2p spectra (Fig. 2b), Co@PCN presents spin orbit doublet at 779.4 eV (Co 2p$_{1/2}$) and 795.4 eV (Co 2p$_{3/2}$) corresponding to metallic cobalt [32], as well as the character peaks of 781.9 and 797.6 eV from Co−N$_x$ configurations [33]. In comparison, the Co 2p spectra of Co-MoN@PCN can only be fitted to Co−N$_x$ (at 782.3 and 798.3 eV), confirming efficient coordinative linkage of atomic Co-N$_x$ based on Co-MoN@PCN. It is found that the Co−N$_x$ signal in Co-MoN@PCN shifts toward high binding energies compared to Co@PCN, indicating an electron deficiency around Co atom in the presence of MoN clusters. The XPS results confirm that the coordination environment of Co atom in Co-MoN@PCN exist not only in Co−N−C but also in Co−N−Mo, consistent with above Raman and FT-IR characterizations. The high-resolution Mo 3d spectra of MoN@CN and Co-MoN@PCN can be deconvoluted into Mo−N bonds (228.6 and 232.5 eV), Mo^{4+} (230.0 and 234.0 eV), and Mo^{6+} (231.7 and 253.3 eV) in Fig. 2c [34]. The Co-MoN@PCN exhibits larger proportion of Mo-N in comparison with MoN@PCN, accompanied by increased Mo^{4+}/Mo^{6+} ratio. This structural evolution depicts that MoN could attract electron density from Co centers, resulting in electron accumulation and decreased valence states of Mo [35,36]. According to the XPS analysis, we can conclude that the surface Co atoms were coordinated and integrated by MoN cluster via Co−N−Mo bonds. Owing to high electrophilicity of MoN, the local electron around Co-N$_x$ was transferred into MoN units through Co−N−Mo bond, resulting in electron deficiency around Co center. This electron transfer can induce the downshift of Co d-band center, thereby improves the adsorption/desorption properties of Co-MoN@PCN catalyst for O$_2$ and its intermediates, achieving fast kinetic and high activity of the integrated Co−N$_x$ sites [37].

X-ray absorption energy near-edge structure (XANES) and extended X-ray absorption fine structure (EXAFS) were carried out to further estimate the local electronic and bonding structures of Co centers. Fig. 2d (with inset enlarged graph) display the K-edge XANES spectra of Co-MoN@PCN, with CoO, Co$_3$O$_4$, CoPc, Co-foil and Co@CN as references. The photon energy of Co-MoN@PCN and Co@PCN are situated between those of CoO and Co$_3$O$_4$, indicating the partial oxidation of Co from valence +2 to +3. It can also be seen that the energy of Co-MoN@PCN are slightly higher than that of Co@CN, indicating higher oxidation state of Co in Co-MoN@PCN [38]. This observation is consistent with the XPS characterization due to electron transfer of MoN-integrated Co-N$_x$. Fourier transform with k^2-weighted EXAFS (FT-EXAFS) spectra was measured to unveil the atomic distribution and coordination environment of Co in Co-MoN@PCN. As shown in Fig. 2e, Co@PCN presents a prominent Co−Co scattering peak at ∼2.14 Å and relatively weak Co−N scattering peak at ∼1.43 Å, revealing the coexistence of metallic Co phase and atomic Co-N$_x$ sites. In contrast, the spectra of Co-MoN@PCN

exhibits only one main peak at ∼1.43 Å, demonstrating that Co primarily exist in single-atomic Co−N$_x$ sites, in good agreement with above STEM and XPS results. Furthermore, wavelet transformed (WT) EXAFS analysis, featured with simultaneous resolution in both *k* and *R* spaces, was used to distinguish atomic species of backscattering atoms. As shown in Fig. 2f, WT contour plots of Co@PCN display intensity maxima at 4.0 Å^{-1} (*R*≈1.4 Å) and 7.40 Å^{-1} (*R*≈1.4 Å), which could be respectively ascribed to Co−N and Co−Co bonding by comparing with CoPc and Co foil. For Co-MoN@PCN, the intensity maximum referring to the Co−Co bonding is visually absent but retain intensity maximum at 4.0 Å^{-1} (*R*≈1.4 Å) distinctly, validating the full coordination and monodispersed structure of Co-N$_x$ sites. The quantitative structural parameters of Co coordination sites were acquired by fitting the Co K-edge FT-EXAFS spectrum in *R* and *k* space (Fig. 2g-h). The best fitting analysis for Co-MoN@PCN consists of Co−N(−C) in the first-shell and Co−N(−Mo) in the second-shell. Specifically, the coordination number (CN) of Co−N(−C) is 2.6 with an average bond length of 1.90 Å, and the CN of Co−N(−Mo) is 1.2 with a bond length of 2.07 Å (see details in Table S1). For comparison, the CN of Co−Co and Co−N(−C) in Co@PCN were estimated to be 2.3 and 4.0 with bond length of 2.39 and 1.90 Å, respectively. The simulation results disclose that in Co-MoN@PCN, the Co-N$_x$ sites were integrated onto MoN clusters by partially forming Co−N−Mo coordination bonding. Compared to previous heteroatom-doping strategy, the POM derivative clusters can not only direct in-situ transition of Co into high-density Co-N$_x$ sites, but also proffer a platform for tuning electronic structures of Co-N$_x$ sites at sub-nanometer scale. It should be also noted that incorporation of Mo$_7$ clusters tends to improve rather than reduce the specific surface area compared to Co@PCN (Fig. S9), which is mainly due to monodispersion of MoN clusters and surface integration of atomic Co against agglomeration. The enhanced surface area would afford rich of accessible atomic Co−N$_x$ sites for efficient catalytic processes.

3.2. Integrating Co-N$_x$ catalytic sites by varied POM clusters

Such a cluster-integrated protocol for Co-N$_x$ catalytic sites has general applicability independent of POM type, shape and size. In addition to Mo$_7$, other types of POM clusters including Na$_2$V$_6$O$_{16}$ (V$_6$), (NH$_4$)$_5$H$_5$[H$_2$W$_6$O$_{24}$] (W$_6$) and Na$_3$PW$_{12}$O$_{40}$ (W$_{12}$) were also applied as intercalates of ECTA to regulate dispersion and linkage of Co(II) within 2D confined space. The XRD patterns of all the catalysts only exhibit the diffraction peaks of POM-derived nitrides (WN and VN, Fig. S10a-c), in the absence of metallic Co. These indicate that the POM and derivative clusters can efficiently prevent aggregation of Co(II) and promote atomic transition into high-density Co-N$_x$ sites. SEM and TEM characterizations (Fig. S10d-i) unveil that the Co-WN@PCN-6/-12 catalysts possess stacked nanosheets structure, while the Co-VN@PCN exhibits nanofibrous structure. The microstructure of the catalysts was clearly identified by HRTEM in Fig. S11. Similar to Co-MoN@PCN, large amounts of WN and VN clusters are monodispersed and evenly distributed within PCN matrix, which is highly beneficial for interfacial coordinating Co(II) and tuning coordination environment of Co-N$_x$ to create high-performance SACs. The effect of POM-derived clusters on dispersing and integrating Co-N$_x$ active sites was evaluated by analyzing the atomic Co content of varied catalysts based on ICP-MS. As revealed in Fig. 4a, the atomic Co contents in the cluster-integrated catalysts are significantly higher (up to 9.9 wt%) than that of Co@PCN catalyst (1.9 wt%), revealing that POM clusters can effectively prevent aggregation tendency of Co and boost atomic distribution of Co−N$_x$ catalytic centers.

3.3. Electrochemical performance for ORR

The electrochemical performance of as-prepared catalysts for ORR was investigated in O$_2$-saturated 0.1 M KOH based on a rotating disk electrode (RDE). As shown in Fig. S12a, the CV curve of Co-MoN@PCN

is virtually featureless when carried out in N_2-saturated electrolyte, while a distinct reduction peak emerges at 0.9 V (vs. RHE) in O_2-saturated electrolyte. Besides, the Co-MoN@PCN manifests more positive cathodic peak than that of Co@PCN (0.80 V) and MoN@CN (0.75 V) (Fig. S12b), suggesting pronounced electrocatalytic activity for ORR. Linear sweep voltammetry (LSV) was further conducted to evaluate the ORR activity of the varied catalysts (Fig. S12c), for which the performance concerning the onset potential (E_{onset}) and half-wave potential ($E_{1/2}$) are compared in Fig. 3b. Particularly, the values of $E_{1/2}$ and E_{onset} are superior to the state-of-the-art Co—N_x single-atom electrocatalysts, as depicted in Fig. 3b and Table S2. Moreover, Co-MoN@PCN shows higher limiting current density among the catalysts, approaching to that of Pt/C. To gain insight into the ORR kinetics, LSV curves of the catalysts were recorded at different rotating speeds from 400 to 2500 rpm (Fig. S13). In comparison with Co@PCN and MoN@CN, Co-MoN@PCN

reveals well-defined plateaux of diffusion-limiting currents below 0.8 V at all rotational speeds, implying efficient surface electrocatalytic reaction with direct four-electron transfer pathways. The corresponding K-L plots of Co-MoN@PCN (Fig. S12d) exhibit good linearity between the current densities and rotation speeds, by which the electron transfer number is determined to be 3.9–4.0 over a wide potential range, revealing the dominant $4e^-$ pathway of direct O_2 reduction to OH^-. Meanwhile, the Co-MoN@PCN displays smallest Tafel slope of 67.4 mV dec^{-1} (Fig. 3c) compared to the MoN@CN (81.6 mV dec^{-1}), Co@PCN (78.1 mV dec^{-1}), verifying the fast ORR kinetics by integration and modulation of Co-N_x site based on MoN clusters.

Rotating ring disk electrode (RRDE) was further employed to assess the electron transfer number and yield of H_2O_2 among the different catalysts (Fig. 3d). The electron transfer number for Co-MoN@PCN is approaching 4 over a wide potential range of 0.2–0.9 V. Also, the H_2O_2
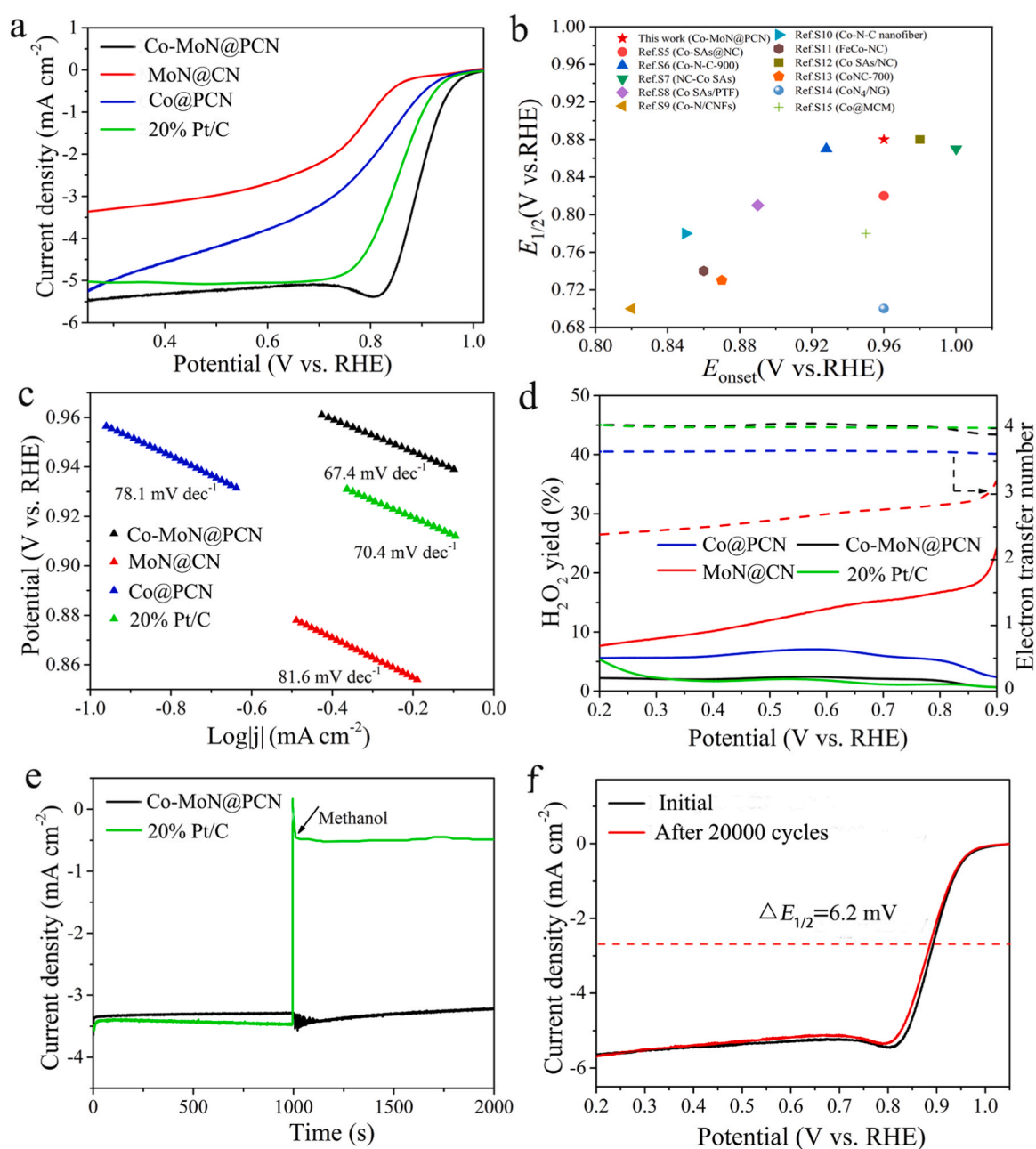

Fig. 3. (a) ORR polarization curves of various catalysts in O_2-saturated 0.1 M KOH with a rotation rate of 1600 rpm, (b) Comparison of E_{onset} and $E_{1/2}$ for various catalysts, (c) Tafel plots, and (d) electron transfer number and H_2O_2 yield for various catalysts, (e) methanol resistance test and (f) ORR polarization plots of Co-MoN@PCN after long-time CV cycling.

yield calculated (~2.5%) is significantly lower than that of Co@PCN (~7.0%) and MoN@CN (~14.1%), demonstrating outstanding selectivity of 4e⁻ ORR pathway of Co-MoN@PCN. In contrast, the lower diffusion-limited currents based on Co@PCN and MoN@CN could be interpreted as the main 2e⁻ ORR pathway with higher H_2O_2 productivity. It is noteworthy that the Co-MoN@PCN possesses much enhanced electrochemical active area (ECSA) compared to Co@PCN and MoN@CN (Fig. S14), suggesting more exposure of surface Co−N_x active sites when integrated onto MoN clusters. The good methanol resistance and durability of Co-MoN@PCN can be evidenced by the chronoamperometric response. As shown in Fig. 3e, no current drop was identified for Co-MoN@PCN in the presence of methanol, revealing the catalyst has high stability against methanol to replace Pt/C catalyst in

methanol fuel cells. The superior stability of Co-MoN@PCN was evidenced by an $E_{1/2}$ loss of only 6.2 mV after 20,000 CV cycles (Fig. 3f). The excellent stability of Co-MoN@PCN can be attributed primarily to integrating Co−N_x sites via robust Co-N-Mo bonds onto MoN clusters, which reinforce the heterostructured active centers and prevent demetallization during ORR process. We further measured the Co content of the catalyst after 20,000 cycles by XPS. It still retained the Co atom ratio of 2.9% that was close to the content before cycling (3.2%), implying less Co leaching during the catalytic process. And the microscopic structure of Co-MoN@PCN after 20,000 CV cycles is characterized by TEM and HRTEM (Fig. S15). It is clear that Co-MoN@PCN retained initial cylinder structure, in which numerous MoN clusters are still in high crystallinity and homogeneously dispersed in PCN, affording stable
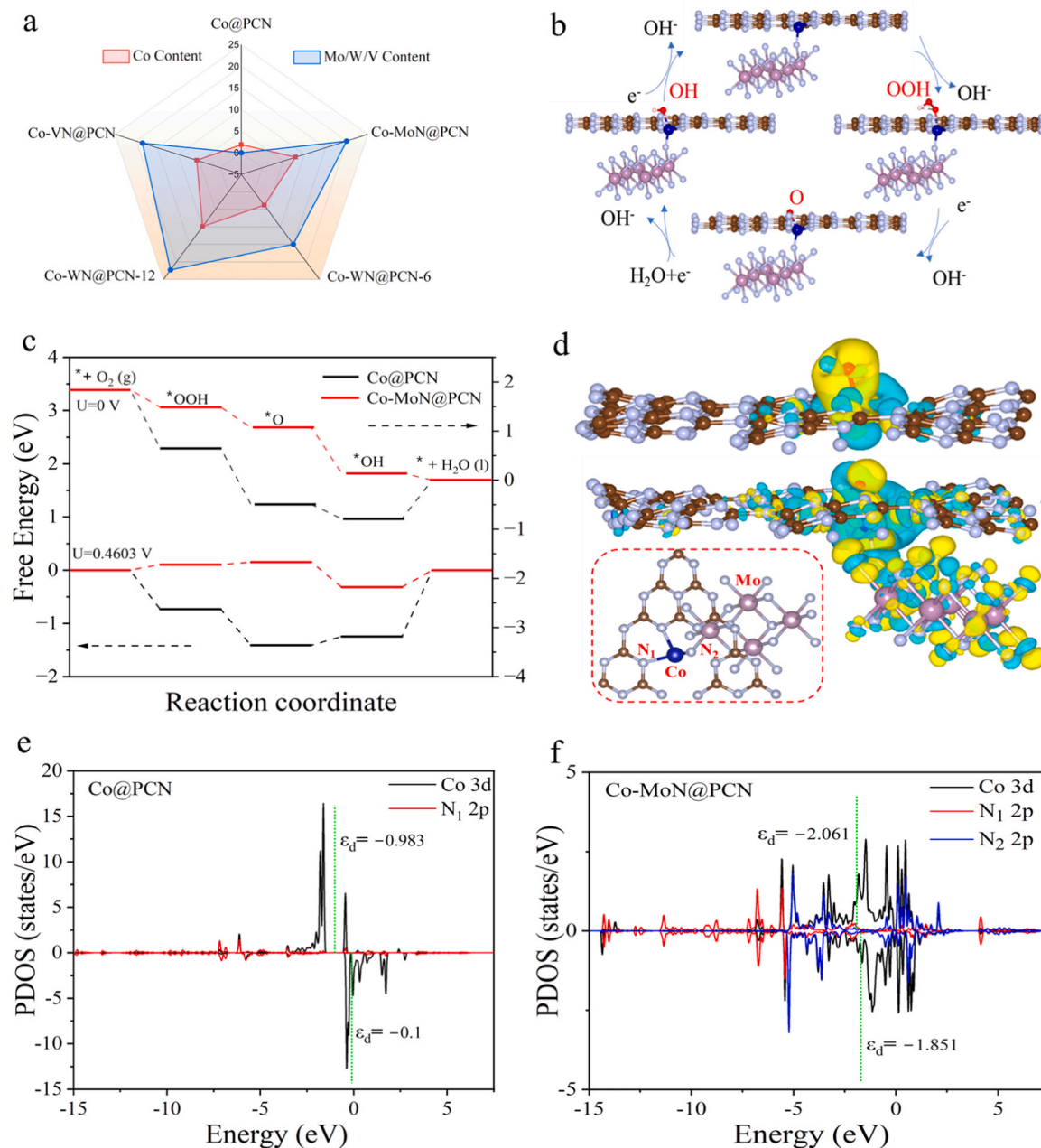

Fig. 4. (a) ICP-MS data on single-atom metal contents between those POM regulated SACs and Co@PCN SACs, (b) Proposed ORR mechanism of Co-MoN@PCN in alkaline media, (c) The free energy diagrams of ORR on Co@PCN and Co-MoN@PCN under the electrode potential of 0 V and 0.4603 V at pH=13, (d) Different charge density distribution of Co@PCN and Co-MoN@PCN sites after OH* adsorption (Cyan and yellow indicate charge depletion and accumulation, respectively), inset reveals the magnified structure of Co-MoN@PCN catalytic site; (e-f) The projected density of states (PDOS) of Co 3d and N 2p based on Co@PCN and Co-MoN@PCN, respectively.

sub-nanometer domains of single-atomic Co-N$_x$ sites.

The integration strategy of Co-N$_x$ sites by POM derivative clusters offers a viable route towards tuning structure and ORR performance of Co-N$_x$ SACs, as proved by the Co-WN@PCN-6/-12 and Co-VN@PCN catalysts. It is remarkable to note that all the POM-derived SACs exhibited more positive E_{onset} and $E_{1/2}$, enhanced steady-state diffusion currents (with diffusion-limiting current plateau) compared to Co@PCN, and mainly four electron transfer number over a large potential range (Fig. S16). Further, the RRDE measurement of the catalysts verified almost four electron transfer processes, with H$_2$O$_2$ yields less than 5% over a broad potential range (Fig. S17a). The WN/VN based SACs also revealed lower Tafel slopes and larger C$_{dl}$ values with respect to Co@PCN (Fig. S17b-f), demonstrating that the SACs integrated by WN/VN clusters possessed more active catalytic sites combining with favorable kinetics. Also, the Co-MoN@PCN exhibited high electrical conductivity of 121 S m^{-1} measured by four-probe method, and lower charge transfer resistance (41 Ω) compared to the Pt/C (49 Ω) using impedance spectroscopy (Fig. S18). These parallel performance testing elucidated the feasibility by incorporating POM and its derivative clusters to simultaneously enhance the atomic loading, activity and conductivity of Co−N$_x$ SACs.

3.4. Theoretical elucidation of MoN-integrated Co-N$_x$ SACs for ORR

To unveil the superior ORR performance upon the effect of integration by POM derivative clusters, DFT calculations were carried out. The structural model of Co-MoN@PCN was optimized and illustrated in Fig. 4b and 4d, on which single Co atom was trapped onto planar C$_3$N$_4$ (in Co-N-C configurations), and simultaneously integrated with MoN clusters via surface N atoms (in Co-N-Mo configurations). Fig. 4b shows the typical proton coupled electron transfer (PCET) steps of Co-MoN@PCN SACs toward ORR in alkaline media, where the first electron transfer step takes place by coupling with one proton from water on the adsorbed O$_2$ to form *OOH; and the *OOH is further reduced into *O, *OH, and eventually H$_2$O by the removal of *OH to complete the PCET cycle. From the corresponding free energy diagrams (Fig. 4c), the ORR steps occurring on the Co-MoN@PCN SACs are all exothermic at the potential of U=0 V (vs. RHE), while the Co@PCN exhibits a strong energy absorption of *OH (0.786 eV). The free energy at the equilibrium U=1.23 V reveal that the rate determining steps on both catalysts are the desorption of *OH (*OH+e$^-$→OH$^-$ +*), where the Co-MoN@PCN has much lower activation barrier of 0.315 eV than Co@PCN (1.247 eV). It is noteworthy that the free energy for *O (ΔG*O) onto Co-N$_x$ centers of Co-MoN@PCN are higher (0.151 eV), which makes the conversion of *O to *OH exothermic, whereas the strong adsorption of *O on Co@PCN leads to a sluggish conversion of *O to *OH. According to the Sabatier principle, the linkage between Co-N$_x$ and MoN can effectively weaken the adsorption capability of metal sites, which promises easy activation and release of O-containing species from the surface, thereby boosting the intrinsic ORR activity. In view of the linear scaling relationship between the intermediates, the electronic interaction between the atomic sites and the adsorbed *OH was analyzed by the charge density difference and Bader charge transfers (Fig. 4d). The Co@PCN exhibits a strong electron transfer (0.51 e) from the Co center to the adsorbed *OH; in contrast, less electron are transformed to *OH (0.37 e) but obviously transferred to MoN (1.64 e) based on Co-MoN@PCN, giving rise to decreased *OH adsorption energy in comparison with Co@PCN. Moreover, the bond distance of Co-N$_2$ (1.617 Å) and Co-N$_1$ (1.887 Å) in the optimized structure of Co-MoN@PCN are generally shorter than the Co-N$_1$ (1.945 Å) in the Co@PCN, validating enhanced stability of Co-N$_x$ sites when integrated by Co-N-Mo bonding. To fundamentally understand the adsorption effects between the two model catalysts, the partial density of states (PDOS) for 3d orbitals of Co and 2p orbitals of N are presented (Fig. 4e-f). Fig. 4e shows the orbital hybridization of Co 3d and N 2p arising from the C$_3$N$_4$ substrate in pyridinic configuration (marked in N$_1$). It is remarkably to note that coordinative linking by

MoN lead to much d-band broadening compared with Co@PCN, demonstrating strengthened d-p orbital hybridization between Co and surface N from MoN (marked in N$_2$) [39]. This state disclosed that distinct from the coordinative N from C$_3$N$_4$ substrates, the unique Co-N-Mo ligand from MoN has a great influence on charge transfer and redistribution between the Co center and surrounding coordination environments. Consequently, the presence of MoN unit leads to significantly downshift of d-band center (ε$_d$, marked in green dash lines) from −0.983/−0.1 eV (Co@PCN) to −2.061/−1.851 eV (Co-MoN@PCN). The much reduced ε$_d$ indicate that more anti-orbitals are occupied in Co center of Co-MoN@PCN. Moreover, after adsorption of *OH, the DOS hybrid orbital area (0→+∞) of Co-MoN@PCN (0.2337) is smaller compared to Co@PCN (0.3378) (Fig. S19), also implying that more antibonding orbital are filled below Fermi level, which is conducive to the resorption and desorption of *OH intermediate and enhance the intrinsic ORR activity. Above analysis by DOS and PDOS are consistent with the calculation on the free energy curves for the speed determination step.

3.5. Bifunctional electrocatalyst for Zn-air batteries application

Taking advantage of the cluster integration and regulation on Co-N$_x$ sites, the Co-MoN@PCN SACs could also be applied for catalyzing oxygen evolution reaction (OER). As shown in Fig. S20, the Co-MoN@PCN exhibits smaller overpotential (340 mV) at the current density of 10 mA cm^{-2} and lower Tafel slope (68.4 mV dec^{-1}) compared to the reference samples, suggesting pronounced electrocatalytic activity and kinetic for OER. The Co-MoN@PCN catalyst manifested excellent ORR and OER performance, thus holding great promise as a cathode dual-functional electrocatalyst for Zn-air batteries (ZABs). Typically, a aqueous ZAB was manufactured by employing Co-MoN@PCN as air cathode, Zn plate as the anode, and 6 M KOH with 0.2 M Zn(CH$_3$COO)$_2$ as an electrolyte (Fig. 5a). For the purpose of comparison, ZAB based on commercial Pt/C and RuO$_2$ (wt (20% Pt/C): wt (RuO$_2$) =1:1) as air cathode (denoted as Pt/C) was also investigated. Obviously, the Co-MoN@PCN ZAB affords a higher open-circuit potential (1.47 V) and lower charge-discharge voltage gap than Pt/C ZAB (Fig. S21), revealing smaller polarization and good recharge capability. Notably, the Co-MoN@PCN ZAB delivered a high peak power density of 176.6 mW cm^{-2} (Fig. 5b), better than the Pt/C ZAB (122.1 mW cm^{-2}). Based on the long-term discharge profiles at 10 mA cm^{-2} (Fig. 5c), the discharge specific capacity (by normalized to the weight of zinc consumption) of Co-MoN@PCN ZAB could reach 755.1 mAh g$_{Zn}^{-1}$, which is higher than that of Pt/C ZAB (735.8 mAh g$_{Zn}^{-1}$). Galvanostatic discharging curves of Co-MoN@PCN ZAB (Fig. 5d) reveals higher discharging voltage at different current densities than Pt/C-based ZAB. When the current density turned back 5 mA cm^{-2}, the discharge potential resumed to 1.33 V, indicating good rate capability and reversibility of Co-MoN@PCN ZAB. The stability of ZABs was assessed by the charge/discharge cycling at a current density of 5 mA cm^{-2}. As displayed in Fig. 5e, the Pt/C based ZAB shows obvious voltage change with enlarged charge−discharge voltage gap from 0.80 to 0.97 V after 78 h; in contrast, the Co-MoN@PCN ZAB retains steady charge−discharge voltage gap from initial 0.88 V to 0.89 V after 100 h cycling, implying excellent stability of Co-MoN@PCN as dual-functional electrocatalysts for ZABs. By comparison with ZABs driven by other non-precious metal catalysts in recent literatures (Table S3), it can be seen that the Co-MoN@PCN ZAB exhibits exceptionally enhanced energy storage performance in terms of power density and specific capacity, indicative of excellent catalytic behavior of Co-MoN@PCN when used in practical ZAB devices.

4. Conclusions

In summary, a cluster integration strategy was demonstrated to effectively regulate the geometric and electronic structures of Co-N$_x$
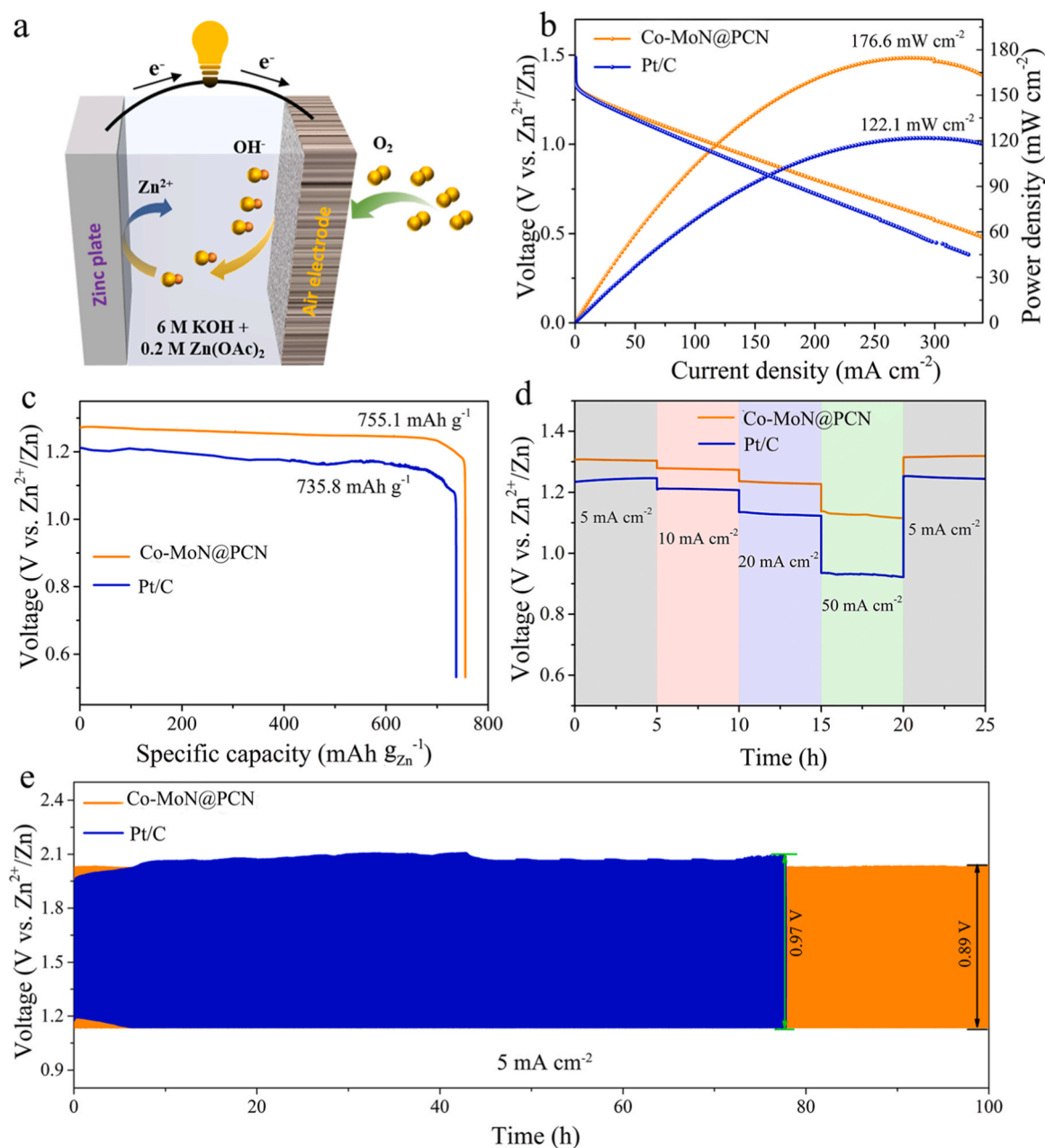
Fig. 5. Electrochemical performance of ZABs based on Co-MoN@PCN and Pt/C (20 wt%) electrocatalysts: (a) Schematic diagram of the assembled ZAB, (b) Polarization and power density curves, (c) Specific capacity normalized with the consumed zinc at 10 mA cm^{-2}, (d) Galvanostatic discharge curves for various current densities, (e) ZAB durability tests at constant current density of 5 mA cm^{-2}.

metal sites, with an aim to promote the atomic site density and activity of Co-N$_x$ type SACs from the sub-nanometer scale. The proposed integration strategy is distinct from the conventional confinement strategy which is less controllable due to the reticular interactions and complex transition processes. Specifically, a variety of POM clusters with sufficient surface oxygen ligands acted as efficient traps to integrate Co atoms onto POM units and prohibited agglomeration of Co atomic sites during pyrolysis to endow abundant Co-N$_x$ single-atom sites in the SACs. The integration of atomic Co based on POM derivative clusters renders a high atomic Co loading up to 9.9 wt%. Compared to common heteroatom doping, the POM derivative clusters (e.g. MoN) imparted strengthened d-p orbital hybridization of Co-N$_x$ sites, which realized to modulate the d-band center and boost the intrinsic activity of Co-N$_x$ SAC from the sub-nanometer scale. Typically, the Co-MoN@PCN catalyst manifests impressive ORR catalytic performance in the alkaline media,

including high activity, outstanding selectivity of 4e$^-$ reaction pathway, and long-term stability. The rechargeable ZAB using Co-MoN@PCN as air electrode delivers a high peak power density (176.6 mW cm^{-2}) and excellent cycling stability. The POM cluster integration strategy expands the methodology toward maximizing the active sites density of M-N$_x$ SACs and offer a viable route to engineer the d orbital hybridization of M-N$_x$ at sub-nanometer level for multiple electrocatalytic applications.

CRediT authorship contribution statement

Shuwen Niu: Writing – original draft, Data curation. **Yunping Wu:** Writing – original draft, Data curation. **Lingzhe Meng:** Investigation. **Zhengyu Wei:** Conceptualization. **Wei Wei:** Writing – review & editing.

Declaration of Competing Interest

The authors declare that they have no known competing financial interests or personal relationships that could have appeared to influence the work reported in this paper.

Data availability

Data will be made available on request.

Acknowledgements

Appendix A. Supporting information

Supplementary data associated with this article can be found in the online version at doi:10.1016/j.apcatb.2024.124014.

References

[1] X. Wan, X. Liu, Y. Li, R. Yu, L. Zheng, W. Yan, H. Wang, M. Xu, J. Shui, Fe–N–C electrocatalyst with dense active sites and efficient mass transport for high-performance proton exchange membrane fuel cells, Nat. Catal. 2 (2019) 259–268, https://doi.org/10.1038/s41929-019-0237-3.

[2] X.X. Wang, M.T. Swihart, G. Wu, Achievements, challenges and perspectives on cathode catalysts in proton exchange membrane fuel cells for transportation, Nat. Catal. 2 (2019) 578–589, https://doi.org/10.1038/s41929-019-0304-9.

[3] X. Duan, S. Ren, N. Pan, M. Zhang, H. Zheng, MOF-derived Fe,Co@N–C bifunctional oxygen electrocatalysts for Zn–air batteries, J. Mater. Chem. A. 8 (2020) 9355–9363, https://doi.org/10.1039/d0ta02825h.

[4] K. Yuan, D. Lützenkirchen-Hecht, L. Li, L. Shuai, Y. Li, R. Cao, M. Qiu, X. Zhuang, M.K.H. Leung, Y. Chen, U. Scherf, Boosting oxygen reduction of single iron active sites via geometric and electronic engineering: nitrogen and phosphorus dual coordination, J. Am. Chem. Soc. 142 (2020) 2404–2412, https://doi.org/10.1021/jacs.9b11852.

[5] J. Su, R. Ge, Y. Dong, F. Hao, L. Chen, Recent progress in single-atom electrocatalysts: concept, synthesis, and applications in clean energy conversion, J. Mater. Chem. A. 6 (2018) 14025–14042, https://doi.org/10.1039/c8ta04064h.

[6] H. Luo, W.J. Jiang, S. Niu, X. Zhang, Y. Zhang, L.P. Yuan, C. He, J.S. Hu, Self-catalyzed growth of Co–N–C nanobrushes for efficient rechargeable Zn–air batteries, Small 16 (2020) 2001171, https://doi.org/10.1002/smll.202001171.

[7] Q. Hu, G. Li, G. Li, X. Liu, B. Zhu, X. Chai, Q. Zhang, J. Liu, C. He, Trifunctional electrocatalysis on dual-doped graphene nanorings–integrated boxes for efficient water splitting and Zn–air batteries, Adv. Energy Mater. 9 (2019) 14, https://doi.org/10.1002/aenm.201803867.

[8] Z. Chen, J. Zhao, C.R. Cabrera, Z. Chen, Computational screening of efficient single-atom catalysts based on graphitic carbon nitride (g-C3N4) for nitrogen electroreduction, Small Methods 3 (2019) 1800368, https://doi.org/10.1002/smtd.201800368.

[9] Y. Leng, S. Du, G. Feng, X. Sang, P. Jiang, H. Li, D. Wang, Cobalt–polypyrrole/melamine-derived Co–N@NC catalysts for efficient base-free formic acid dehydrogenation and formylation of quinolines through transfer hydrogenation, ACS Appl. Mater. Interfaces 12 (2019) 474–483, https://doi.org/10.1021/acsami.9b14839.

[10] Y. Zhu, J. Sokolowski, X. Song, Y. He, Y. Mei, G. Wu, Engineering local coordination environments of atomically dispersed and heteroatom-coordinated single metal site electrocatalysts for clean energy-conversion, Adv. Energy Mater. 10 (2020) 1902844, https://doi.org/10.1002/aenm.201902844.

[11] K. Huang, L. Zhang, T. Xu, H. Wei, R. Zhang, X. Zhang, B. Ge, M. Lei, J.-Y. Ma, L.-M. Liu, H. Wu, −60 °C solution synthesis of atomically dispersed cobalt electrocatalyst with superior performance, Nat. Commun. 10 (2019) 606, https://doi.org/10.1038/s41467-019-08484-8.

[12] Z. Yu, C. Si, A.P. LaGrow, Z. Tai, W.A. Caliebe, A. Tayal, M.J. Sampaio, J.P. S. Sousa, I. Amorim, A. Araujo, L. Meng, J.L. Faria, J. Xu, B. Li, L. Liu, Iridium–iron diatomic active sites for efficient bifunctional oxygen electrocatalysis, ACS Catal. 12 (2022) 9397–9409, https://doi.org/10.1021/acscatal.2c01861.

[13] Z. Zhu, H. Yin, Y. Wang, C.H. Chuang, L. Xing, M. Dong, Y.R. Lu, G. Casillas-Garcia, Y. Zheng, S. Chen, Y. Dou, P. Liu, Q. Cheng, H. Zhao, Coexisting single-atomic Fe and Ni sites on hierarchically ordered porous carbon as a highly efficient ORR electrocatalyst, Adv. Mater. 32 (2020) 2004670, https://doi.org/10.1002/adma.202004670.

[14] X. Xie, C. He, B. Li, Y. He, D.A. Cullen, E.C. Wegener, A.J. Kropf, U. Martinez, Y. Cheng, M.H. Engelhard, M.E. Bowden, M. Song, T. Lemmon, X.S. Li, Z. Nie, J. Liu, D.J. Myers, P. Zelenay, G. Wang, G. Wu, V. Ramani, Y. Shao, Performance enhancement and degradation mechanism identification of a single-atom Co–N–C catalyst for proton exchange membrane fuel cells, Nat. Catal. 3 (2020) 1044–1054, https://doi.org/10.1038/s41929-020-00546-1.

[15] H. Tian, A. Song, P. Zhang, K. Sun, J. Wang, B. Sun, Q. Fan, G. Shao, C. Chen, H. Liu, Y. Li, G. Wang, High durability of Fe–N–C single-atom catalysts with carbon vacancies toward the oxygen reduction reaction in alkaline media, Adv. Mater. 35 (2023) 2210714, https://doi.org/10.1002/adma.202210714.

[16] L.J. Yuan, B. Liu, Lx Shen, Y.K. Dai, Q. Li, C. Liu, W. Gong, X.L. Sui, Z.B. Wang, d-Orbital electron delocalization realized by axial Fe4C atomic clusters delivers high-performance Fe–N–C catalysts for oxygen reduction reaction, Adv. Mater. 35 (2023) 2305945, https://doi.org/10.1002/adma.202305945.

[17] Y. Chen, S. Ji, Y. Wang, J. Dong, W. Chen, Z. Li, R. Shen, L. Zheng, Z. Zhuang, D. Wang, Y. Li, Isolated single iron atoms anchored on N-doped porous carbon as an efficient electrocatalyst for the oxygen reduction reaction, Angew. Chem. Int. Ed. 56 (2017) 6937–6941, https://doi.org/10.1002/anie.201702473.

[18] Y. Ha, B. Fei, X. Yan, H. Xu, Z. Chen, L. Shi, M. Fu, W. Xu, R. Wu, Atomically dispersed Co-pyridinic N-C for superior oxygen reduction reaction, Adv. Energy Mater. 10 (2020) 2002592, https://doi.org/10.1002/aenm.202002592.

[19] Z. Lin, A. Yang, B. Zhang, B. Liu, J. Zhu, Y. Tang, X. Qiu, Coupling the atomically dispersed Fe-N3 sites with sub-5 nm Pd nanocrystals confined in N-doped carbon nanobelts to boost the oxygen reduction for microbial fuel cells, Adv. Funct. Mater. 32 (2021) 2107683, https://doi.org/10.1002/adfm.202107683.

[20] Q. Wang, Y. Yang, F. Sun, G. Chen, J. Wang, L. Peng, W.T. Chen, L. Shang, J. Zhao, D. Sun-Waterhouse, T. Zhang, G.I.N. Waterhouse, Molten NaCl-assisted synthesis of porous Fe-N-C electrocatalysts with a high density of catalytically accessible FeN4 active sites and outstanding oxygen reduction reaction performance, Adv. Energy Mater. 11 (2021) 2100219, https://doi.org/10.1002/aenm.202100219.

[21] X. Xie, L. Shang, X. Xiong, R. Shi, T. Zhang, Fe single-atom catalysts on MOF-5 derived carbon for efficient oxygen reduction reaction in proton exchange membrane fuel cells, Adv. Energy Mater. 12 (2021) 2102688, https://doi.org/10.1002/aenm.202102688.

[22] S. Yuan, J. Zhang, L. Hu, J. Li, S. Li, Y. Gao, Q. Zhang, L. Gu, W. Yang, X. Feng, B. Wang, Decarboxylation-induced defects in MOF-derived single cobalt atom@carbon electrocatalysts for efficient oxygen reduction, Angew. Chem. Int. Ed. 60 (2021) 21685–21690, https://doi.org/10.1002/anie.202107053.

[23] L. Jiao, R. Zhang, G. Wan, W. Yang, X. Wan, H. Zhou, J. Shui, S.-H. Yu, H.-L. Jiang, Nanocasting SiO2 into metal–organic frameworks imparts dual protection to high-loading Fe single-atom electrocatalysts, Nat. Commun. 11 (2020) 2831, https://doi.org/10.1038/s41467-020-16715-6.

[24] Z. Liang, N. Kong, C. Yang, W. Zhang, H. Zheng, H. Lin, R. Cao, Highly curved nanostructure-coated Co, N-doped carbon materials for oxygen electrocatalysis, Angew. Chem. Int. Ed. 60 (2021) 12759–12764, https://doi.org/10.1002/anie.202101562.

[25] C. Ouyang, L. Zheng, Q. Zhang, X. Wang, A simple preheating-pyrolysis strategy leading to superior oxygen reduction reaction activity in Fe-N/carbon black, Adv. Mater. 34 (2022) 2205372, https://doi.org/10.1002/adma.202205372.

[26] D. Xia, X. Tang, S. Dai, R. Ge, A. Rykov, J. Wang, T.H. Huang, K.W. Wang, Y. Wei, K. Zhang, J. Li, L. Gan, F. Kang, Ultrastable Fe–N–C fuel cell electrocatalysts by eliminating non-coordinating nitrogen and regulating coordination structures at high temperatures, Adv. Mater. 35 (2022) 2204474, https://doi.org/10.1002/adma.202204474.

[27] C.C.L. McCrory, S. Jung, J.C. Peters, T.F. Jaramillo, Benchmarking heterogeneous electrocatalysts for the oxygen evolution reaction, J. Am. Chem. Soc. 135 (2013) 16977–16987, https://doi.org/10.1021/ja407115p.

[28] T. Ouyang, Y.Q. Ye, C.Y. Wu, K. Xiao, Z.Q. Liu, Heterostructures composed of N-doped carbon nanotubes encapsulating cobalt and beta-Mo2C nanoparticles as bifunctional electrodes for water splitting, Angew. Chem. Int. Ed. Engl. 58 (2019) 4923–4928, https://doi.org/10.1002/anie.201814262.

[29] Y. Yan, H. Li, Y. Cheng, T. Yan, W. Gao, J. Mao, K. Dai, L. Zhang, Boosting polysulfide redox conversion of Li-S batteries by one-step-synthesized Co-Mo bimetallic nitride, J. Energy Chem. 61 (2021) 336–346, https://doi.org/10.1016/j.jechem.2021.03.041.

[30] G. Ran, J. Yang, Y. Xing, Y. Zhang, X. Tang, Q. Hu, K. Huang, Z. Zou, H. Yu, X. Xiong, A novel Co3Mo3N self-embedded in porous carbon nanocomposite derived from Mo doped ZIF-67: an effective catalyst for electrochemical H2O2 sensing, Microchem. J. 185 (2023) 108296, https://doi.org/10.1016/j.microc.2022.108296.

[31] I.S. Amiinu, Z. Pu, X. Liu, K.A. Owusu, H.G.R. Monestel, F.O. Boakye, H. Zhang, S. Mu, Multifunctional Mo-N/C@MoS2 electrocatalysts for HER, OER, ORR, and Zn-Air batteries, Adv. Funct. Mater. 27 (2017) 1702300, https://doi.org/10.1002/adfm.201702300.

[32] W.L. Jiarui He, Yuanfu Chen, Jie Xiong, Kechun Wen, Chen Xu, Wanli Zhang, Yanrong Li, Wu Qin, Weidong He, Direct impregnation of SeS2 into a MOF-derived 3D nanoporous Co–N–C architecture towards superior rechargeable lithium batteries, J. Mater. Chem. A 6 (2018) 10466, https://doi.org/10.1039/C8TA02434K.

[33] X. Huang, W. Liu, J. Zhang, M. Song, C. Zhang, J. Li, J. Zhang, D. Wang, Coupling Co-N-C with MXenes yields highly efficient catalysts for H2O2 production in acidic media, ACS Appl. Mater. Interfaces 14 (2022) 11350–11358, https://doi.org/10.1021/acsami.1c22641.

[34] H. Shi, T.Y. Dai, W.B. Wan, Z. Wen, X.Y. Lang, Q. Jiang, Mo-/Co-N-C hybrid nanosheets oriented on hierarchical nanoporous Cu as versatile electrocatalysts for efficient water splitting, Adv. Funct. Mater. 31 (2021) 2102285, https://doi.org/10.1002/adfm.202102285.

[35] T. Sun, Q. Wu, R. Che, Y. Bu, Y. Jiang, Y. Li, L. Yang, X. Wang, Z. Hu, Alloyed Co–Mo nitride as high-performance electrocatalyst for oxygen reduction in acidic medium, ACS Catal. 5 (2015) 1857–1862, https://doi.org/10.1021/cs502029h.

[36] J. Sun, W. Xu, C. Lv, L. Zhang, M. Shakouri, Y. Peng, Q. Wang, X. Yang, D. Yuan, M. Huang, Y. Hu, D. Yang, L. Zhang, Co/MoN hetero-interface nanoflake array with enhanced water dissociation capability achieves the Pt-like hydrogen evolution catalytic performance, Appl. Catal. B: Environ. 286 (2021) 119882, https://doi.org/10.1016/j.apcatb.2021.119882.

[37] X.P. Han, W. Zhang, X.Y. Ma, C. Zhong, N.Q. Zhao, W.B. Hu, Y.D. Deng, Identifying the activation of bimetallic sites in NiCo$_2$S$_4$@g-C$_3$N$_4$-CNT hybrid electrocatalysts for synergistic oxygen reduction and evolution, Adv. Mater. 31 (2019) 1808281, https://doi.org/10.1002/adma.201808281.

[38] L. Li, X. Tang, S. Huang, C. Lu, D. Lützenkirchen-Hecht, K. Yuan, X. Zhuang, Y. Chen, Longitudinally grafting of graphene with iron phthalocyanine-based porous organic polymer to boost oxygen electroreduction, Angew. Chem. Int. Ed. 62 (2023) e2023016, https://doi.org/10.1002/anie.202301642.

[39] H. Chen, Q. Wu, Y. Wang, Q. Zhao, X. Ai, Y. Shen, X. Zou, d–sp orbital hybridization: a strategy for activity improvement of transition metal catalysts, Chem. Commun. 58 (2022) 7730–7740, https://doi.org/10.1039/d2cc02299k.